9-2023

The effect of slow strain rate tension and cyclic loading on biodegradable Zn–2%Fe–0.8%Mn alloy in a simulated physiological environment

Lital Ben Tzion-Mottye
Ben-Gurion University of the Negev

Adi Bahar
Ben-Gurion University of the Negev

Tomer Ron
Ben-Gurion University of the Negev

Galit Katarivas Levy
Ben-Gurion University of the Negev

Jeremy Goldman
Michigan Technological University, jgoldman@mtu.edu

See next page for additional authors

Recommended Citation

Ben Tzion-Mottye, L., Bahar, A., Ron, T., Katarivas Levy, G., Goldman, J., Eliezer, D., & Aghion, E. (2023). The effect of slow strain rate tension and cyclic loading on biodegradable Zn–2%Fe–0.8%Mn alloy in a simulated physiological environment. *Journal of Materials Research and Technology, 26*, 8527-8540. http://doi.org/10.1016/j.jmrt.2023.09.178
Retrieved from: https://digitalcommons.mtu.edu/michigantech-p2/197

Follow this and additional works at: https://digitalcommons.mtu.edu/michigantech-p2

 Part of the Biomedical Engineering and Bioengineering Commons

Available online at www.sciencedirect.com

jmr&t Journal of Materials Research and Technology

journal homepage: www.elsevier.com/locate/jmrt

The effect of slow strain rate tension and cyclic loading on biodegradable Zn–2%Fe–0.8%Mn alloy in a simulated physiological environment

Lital Ben Tzion-Mottye [a], *Adi Bahar* [a], *Tomer Ron* [a,*], *Galit Katarivas Levy* [b], *Jeremy Goldman* [c], *Dan Eliezer* [a], *Eli Aghion* [a]

[a] Department of Materials Engineering, Ben-Gurion University of the Negev, Beer-Sheva 8410501, Israel
[b] Department of Biomedical Engineering, Ben-Gurion University of the Negev, Beer-Sheva 8410501, Israel
[c] Biomedical Engineering Department, Michigan Technological University, Houghton, MI, USA

ARTICLE INFO

Article history:
Received 19 July 2023
Accepted 18 September 2023
Available online 21 September 2023

Keywords:
Biodegradable implants
Cell viability
In vitro
Zinc
Corrosion fatigue
Slow strain rate testing

ABSTRACT

Zinc-based alloys have gained increased interest as biodegradable structural materials for medical applications due to their adequate biocompatibility, crucial roles in many physiological functions and attractive antibacterial properties. However, the major drawbacks of zinc alloys relate to their inadequate mechanical properties and tendency to provoke fibrous encapsulation due to relatively high standard potential. Based on the promising effect of Mn on properties of Zn-based alloys, the present study aimed at evaluating the suitability of Zn–2%Fe–0.8%Mn alloy as a potential biodegradable implant under in-vitro conditions. This evaluation focused on the passivation characteristics as determined by cyclic potentiodynamic polarization analysis, immersion test, stress corrosion behavior by slow strain rate testing (SSRT), corrosion fatigue and direct cell viability in terms of cell adherence and proliferation after 24 and 48 h post incubation. The results showed that the addition of 0.8%Mn to the base Zn–2%Fe alloy improves the specific strength and direct cell viability characteristics while decreasing the effectiveness of natural passivation processes. The main overall effect of adding 0.8%Mn to Zn–2%Fe alloy were (i) reduced stress corrosion resistance in terms of time to failure at a low strain rate (2.5×10^{-7} s^{-1}) from 285 h to 205 h (ii) reduced corrosion fatigue endurance from 4,997,285 cycles to only 377,552 cycles to failure at the lowest load of 30 MPa.

1. Introduction

Zn-based alloys can be considered as attractive structural materials for biodegradable implants that can replace permanent implants such as Ti-base alloys, stainless steels, and cobalt-based alloys [1]. The replacement of permanent implants can avoid their undesirable side effects of chronic inflammation and long-term mechanical failure in orthopedic and cardiovascular applications. Mg alloys remain the most promising biodegradable alternative to Zn-based alloys. However, Mg-based alloys suffer from accelerated corrosion degradation mainly due to the reduced standard potential of

* Corresponding author.
E-mail address: toron@post.bgu.ac.il (T. Ron).
https://doi.org/10.1016/j.jmrt.2023.09.178

pure Mg (−2.372 V) and the inherent danger of gas embolism [2–5]. Comparatively, pure Zn has a higher standard potential (−0.762 V) and consequently reduced rates of corrosion. Furthermore, Zn does not produce hydrogen gas upon degradation [6–8].

The construction of biodegradable implants based on zinc is justified by the myriad physiological roles for zinc in the human body. Zn is a key element in various biological processes such as nucleic acid metabolism, gene expression and cell growth. The daily intake of Zn is 15 mg/day and its concentration within the human body is regulated by the kidneys [9,10]. Unfortunately, pure Zn suffers from poor mechanical properties (tensile strength 20 MPa and 0.2% elongation) relative to conventional metallic implants [11]. To address this drawback several Zn-based alloys have been recently developed and examined including Zn-Ti [12], Zn–Mg–Mn [13,14], Zn-Cu and Zn–Cu–Ti [15]. In addition, Zn-base alloys tend to suffer from an insufficient rate of degradation. Arterial implants that degrade too slowly are at risk of fibrous encapsulation, which limits their successful tissue integration [16,17]. This particular drawback was addressed by developing Zn-based alloys with alloying elements that can induce galvanic corrosion, such as Zn-Fe [18,19] and Zn–Fe–Ca [20]. The resulting galvanic corrosion can be made relatively uniform with finely dispersed precipitates. Another challenge of Zn-based alloys relates to their performance under stress corrosion and corrosion fatigue conditions. Such environments exist for implants placed under continuous or cyclic stress from normal human body functions and vary depending upon the specific implant site [24]. Vulnerabilities in accommodating cyclic loading can provoke premature failure of the implant [21–23].

The present study aims at examining the stress corrosion behavior and corrosion fatigue of biodegradable Zn–2% Fe–0.8%Mn alloy under in-vitro conditions. This includes direct cell viability analysis to evaluate the biocompatibility of the alloy. The use of Fe and Mn as alloying elements is justified based on their vital role in normal body functioning. The recommended daily intake is 8–18 mg and 0.6–5 mg for Fe and Mn, respectively [25,26]. Furthermore, Fe is an essential element of several metalloproteins and is vital for biochemical activities [27–29] while Mn is an activator of enzyme systems and its deficiency can lead to diabetes, osteoporosis and atherosclerosis [9,30,31]. Therefore, the dissolution of these alloy components into metallic ions is not expected to produce a harmful systemic effect.

2. Experimental

2.1. Preparation of tested alloy

The tested alloy in the form of a biodegradable Zn-base system having the composition of Zn–2%Fe–0.8%Mn was produced by a gravity casting process. The use of 0.8%Mn was in accordance with the solubility limit in pure Zn as well as brittleness concerns [32] and strength requirements [33]. The casting procedure was performed using a graphite crucible and pure Zn bars along with Fe and Mn powders with average particle sizes of 40–50 μm. The melting and alloying process was carried out at 700 °C for 2 h while stirring every 30 min. The molten alloy was cast in a cylindrical steel die to obtain alloy bars with dimensions of 16 cm length and 6 cm diameter that were then homogenized at 200 °C for 2 h. The tested alloy was then extruded at 400 °C to obtain final rods with 6 mm diameter.

2.2. Microstructure examination

As part of the metallography analysis, the tested alloy was polished and etched in 5% Nital solution (100 mL HNO_3 + 100 mL ethanol). The general microstructure of the alloy post extrusion was evaluated by scanning electron microscopy (SEM), JEOL JSM-5600 (JEOL, Tokyo, Japan). Further investigation was carried out using transmission electron microscopy (TEM) (JEOL JEM-2100F, Jeol Ltd., Tokyo, Japan) operating at 200 kV. This investigation involved bright field imaging, selected area electron diffraction (SAED) and EDS analysis for local chemical composition. Cross-sectional specimens were produced using a dual-beam focused ion beam microscope (FEI, Verios-460L, Hillsboro, OR USA).

2.3. Corrosion resistance and electrochemical behavior

The corrosion resistance of the tested alloys was examined by means of immersion test in PBS solution at 37 °C for 7 days. The corrosion products were removed using ethanol and ultrasonic bath while the weight loss and corresponding corrosion rate were defined according to ASTM G2 standard. Following the immersion tests the external surfaces of the corroded samples were examined using SEM analysis.

The electrochemical behavior of the tested alloy in the form of cyclic potentiodynamic polarization was carried out using a Bio-Logic SP-200 potentiostat (BioLogic Science Instruments, Seyssinet-Pariset, France), equipped with EC-Lab software V11.18. This analysis was performed using a three-electrode cell including the tested alloy as a working electrode with an exposed area of 0.28 cm, a platinum counter electrode, and a saturated calomel (SCE) as a reference electrode. The corrosive medium was in the form of PBS solution at room temperature. The corrosion rate of the tested alloy was evaluated using Tafel extrapolation.

2.4. Stress corrosion analysis by slow strain rate testing (SSRT)

SSRT analysis is used to evaluate the susceptibility of alloys to stress corrosion cracking that can take place under a combined effect of a corrosive environment and mechanical loading. SSRT is also known as constant extension rate testing (CERT) as it involves testing specimens in tensile conditions and usually at relatively low strain rates. In this study, the SSRT analysis was carried out using a Cormet C-76 apparatus (Cormet Testing Systems, Vantaa, Finland). The tested samples in the form of rods had a dimeter of 5.6 mm and length of 50 mm. The gauge length and diameter were 18 mm and 3.6 mm respectively. The strain rates used were between 2.5×10^{-5} and 2.5×10^{-7} s^{-1}, which can simulate a reduced and increased effect of the corrosive medium, correspondingly. The corrosive environment was standard PBS solution at 37 °C to simulate in-vivo thermal conditions.

2.5. Corrosion fatigue examination

The corrosion fatigue performance of the tested alloys was examined using a SM1019 rotating fatigue machine (Tec-Quipment Ltd., Nottingham, U.K.). The results were introduced in terms of S–N curves. The specimens' neck diameter was 4 mm and the total length was 64 mm. The fatigue tests were carried out using a load range of 30–230 MPa at 30 Hz in both air and a corrosive atmosphere to evaluate the effect of the simulated physiological environment. The corrosive environment was obtained by continuously dropping PBS solution onto the neck section during cyclic loading.

2.6. Direct cell viability analysis

Direct cell testing was performed to evaluate cell viability and adhesion on tested alloys surfaces using Mus musculus (mouse) 4T1 cells. Sample preparation and test protocols were carried out according to ISO 10993-5/12 standards [34,35]. The cells were cultured in an incubator under a humid atmosphere containing 5% CO2 at 37 °C using Dulbecco Modified Eagle's Medium (DMEM) supplemented with 4.5 g/L D-Glucose, 10% Fetal Bovine Serum (FBS), 4 mM L-Glutamine, 1 mM Sodium Pyruvate, and 1% Penicillin Streptomycin Neomycin (PSN) antibiotic mixture (Biological Industry, Beit Haemek, Israel). Cylindrical samples with a diameter of 10 mm and height of 2 mm were made from the tested alloy Zn–2%Fe–0.8%Mn as well as from Zn–2%Fe and Ti–6Al–4V alloys that acted as reference substances. For statistical consideration, 8 samples from each alloy were used for two independent repetitions of the experiment. The samples were polished to 2500 grit, cleaned ultrasonically for 5 min in ethanol and 2 min in acetone, air-dried, and then sterilized in an autoclave. All the samples were pre-incubated for 24 h in Dulbecco Modified Eagle's Medium (DMEM) at 37 °C in a humid atmosphere. The surface area to volume ratio of the culture medium was 1.25 cm^2/mL according to standards. After 24 h of pre-incubation, the samples were placed in 24-well culture plates and cells were seeded directly onto the alloy surface at a density of 100,000 cells per well. This was followed by an additional incubation of 3 h to allow cell adhesion to the surface. More DMEM was added to each well according to the standard ratio. Finally, the plates were incubated in a humid atmosphere containing 5% CO2 at 37 °C for 24 and 48 h.

To visualize the number of adherent cells, a NucBlue™ Live Cell Stain Formulation kit (RHENIUM, Modi'in, Israel) was used. The results were documented by a CoolLED pe-2 collimator fitted to an inverted phase-contrast microscope (Eclipse Ti, Nikon) equipped with a digital camera (D5-Qi1Mc, Nikon, Tokyo, Japan) using the appropriate fluorescent filters. Cell adhesion was quantified by averaging cell counts at three random spots on the sample surface.

The evaluation of cell viability was performed using a Live and Dead Cell Assay (Abcam, Cambridge, UK) according to the manufacturer's protocol. The Live and Dead Assay stain solution was made of two dyes that allow the differentiation

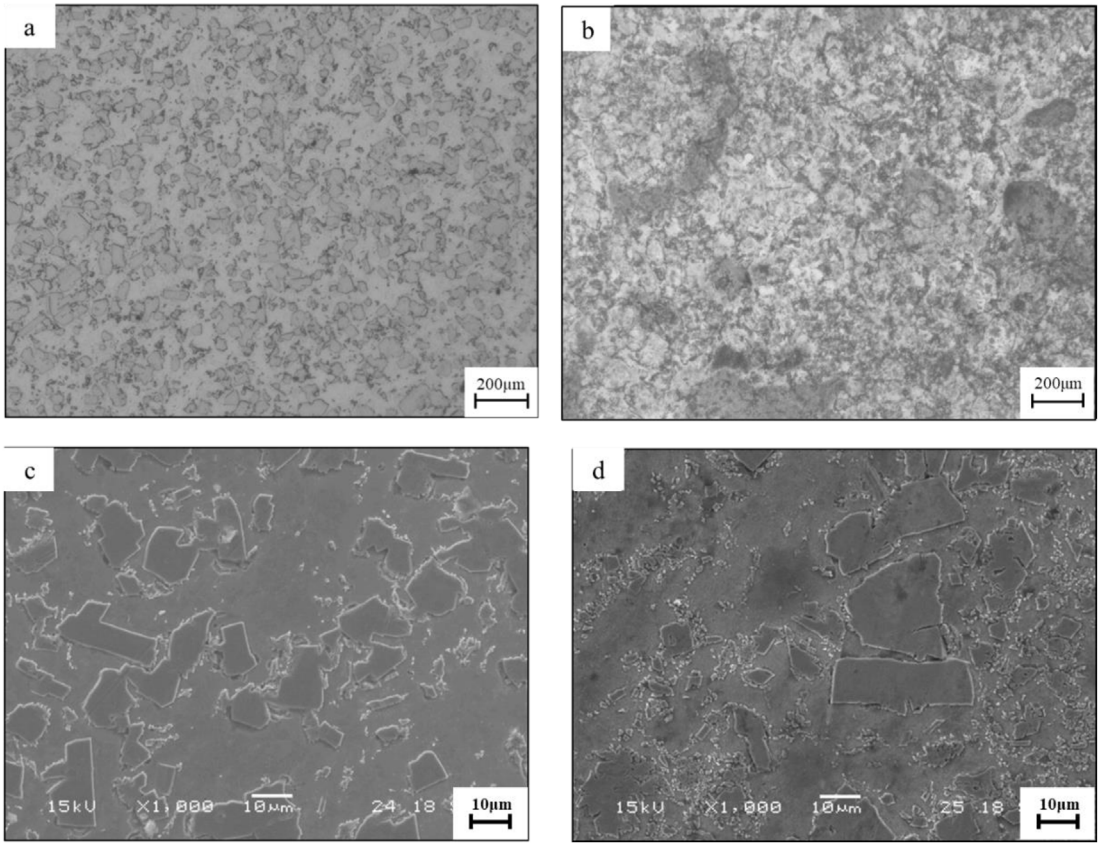

Fig. 1 – Optical microscopy and Scanning electron microscopy (SEM) post extrusion of (a), (c) Zn–2%Fe and (b), (d) Zn–2% Fe–0.8%Mn.

between live and dead cells. The viable cells were shown as green (Excitation and Emission of 494 nm and 515 nm, respectively), while the dead cells were shown as red (Excitation and Emission of 528 nm and 617 nm, respectively).

3. Results

The effect of 0.8%Mn addition on the Zn–2%Fe alloy microstructure is shown in Fig. 1 by optical and electron microscopy, respectively. Both alloys exhibited a homogenized microstructure with a preferred orientation, as expected after an extrusion process. The Zn–2%Fe alloy included a main precipitate $Zn_{11}Fe$ with a blocky appearance [19] while the Zn–2%Fe–0.8%Mn alloy contained an additional secondary phase in the form of (Fe, Mn) Zn_{13} [31,33,36]. This secondary phase forms because Fe and Mn both have a BCC structure with only about 3% difference in atomic radii (156 p.m. and 161 p.m., respectively). Hence, Mn atoms can substitute with Fe atoms in this composed phase.

In-depth examination of Zn–2%Fe–0.8%Mn alloy by high resolution TEM and SAED analysis is presented in Fig. 2 along with the EDS analysis, which is shown in Table 1. This has identified the presence of an additional δ_{1p} phase with a hexagonal structure, $Zn_{126}Fe_{13}$ [37,38]. The presence of this phase comes in line with the basic phase composition introduced by Raghavan [44] in relation to Zn–Fe–Mn ternary system. Accordingly, apart from the (Fe, Mn) Zn_{13} phase obtained by the XRD analysis, two other phases can exist, δ and ξ phase [45]. In addition, the localized composition at the interface between the δ phase and the matrix included a relatively abnormal amount of Mn (3%) that have probably segregated to this region as indicated in Table 1 (point 1).

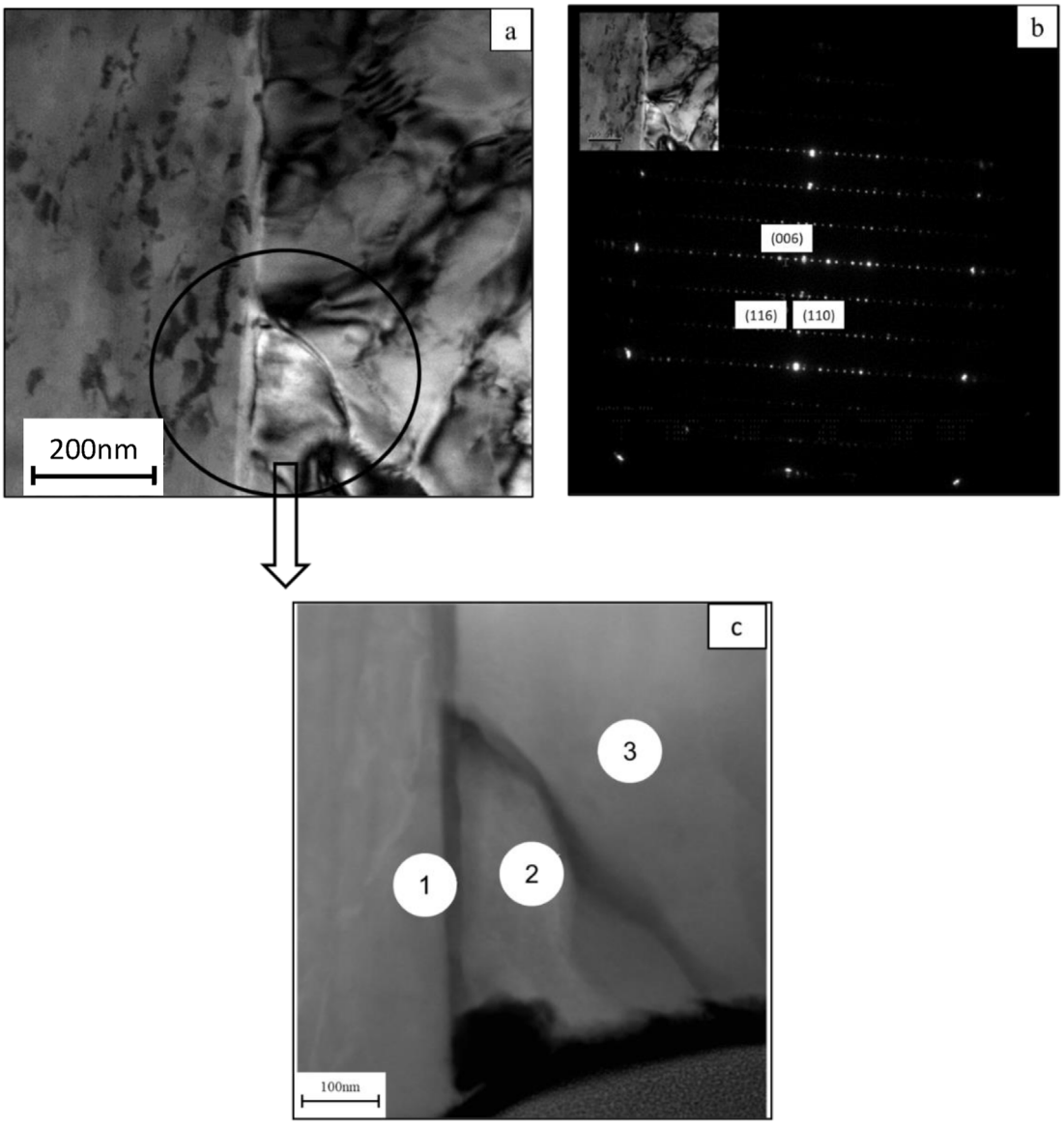

Fig. 2 – (a) Close-up view by TEM of a secondary precipitate phase in Zn–2%Fe–0.8%Mn alloy; (b) SAED analysis of the secondary precipitate; (c) Measurement points by EDS analysis.

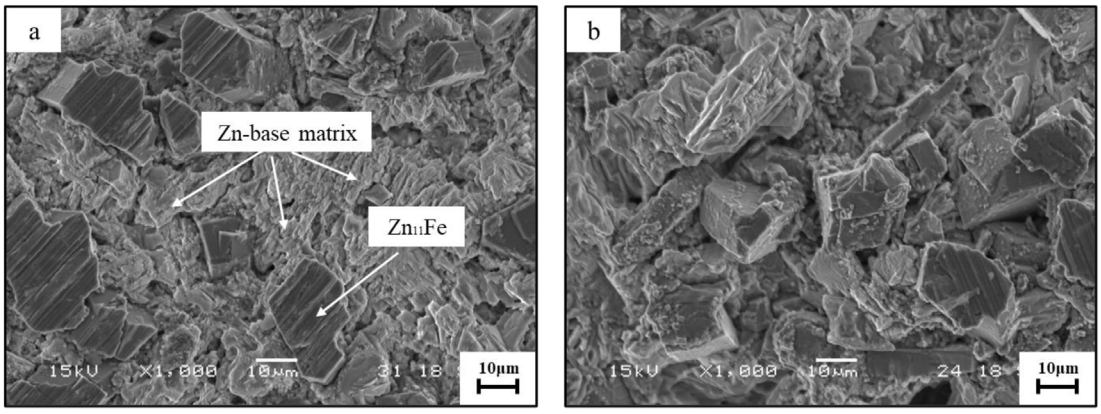

Fig. 3 – External surface appearance of the tested alloys post immersion experiment in PBS solution at 37 °C for 14 days (a) Zn–2%Fe (b) Zn–2%Fe–0.8%Mn.

Table 1 – Chemical composition as obtained by EDS analysis at selected areas shown in Fig. 3c.

Point of measurement	Zn	Fe	Mn	Dominant phase
1	89.77	7.22	3.01	δ_{1p} phase
2	98.85	0.48	0.67	Zn matrix
3	98.65	0.42	0.92	Zn matrix

Table 2 – Tafel extrapolation measurements.

	Zn–2%Fe	Zn–2%Fe–0.8%Mn
Ecorr [V]	−1.150	−1.133
Icorr [µA]	0.262	0.568
C.R [mmpy]	0.003	0.008

The corrosion resistance in terms of immersion test showed that the average corrosion rate of Zn–2%Fe–0.8%Mn was relatively higher compared to its counterpart alloy without Mn, 0.53 vs. 0.50 mm/year respectively. The external surface appearance of the tested alloys post immersion test is shown in Fig. 3. This have revealed that the main precipitate phase ($Zn_{11}Fe$) having a blocky shape and sharp edges in the base alloy Zn–2%Fe was un-attacked. Comparatively, the parallel precipitate in the Zn–2%Fe–0.8%Mn alloy was slightly attacked especially at the edges. This can be partly explained by the TEM analysis (Fig. 3 and Table 1) that highlight the

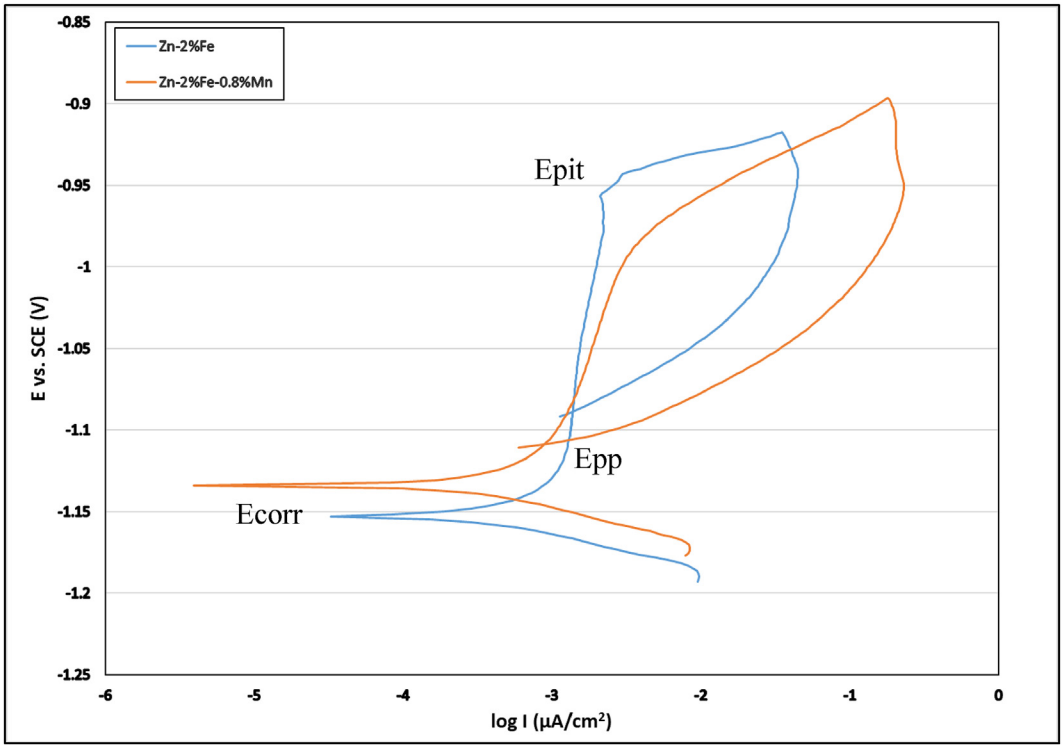

Fig. 4 – Typical cyclic polarization analysis in PBS solution.

presence of abnormal segregation of Mn at the interface of the precipitating phases. Consequently, it is believed that the preferred segregation of Mn can create additional micro-galvanic corrosion that can be generated due to the inherent differences in standard potential between Mn and Zn (−1.18 V and −0.763 V respectively).

The sensitivity of the tested alloys to localized corrosion attack in terms of cyclic potentiodynamic polarization analysis is shown in Fig. 4. Table 2 presents the Tafel extrapolation measurements. The hysteresis curve path of the two alloys showed a decreased potential that eventually crosses the polarization curve at the passive region. This represents the typical behavior of a metal that undergoes some type of localized corrosion attack [39]. Furthermore, the pitting potential (Epit) of the alloy containing 0.8%Mn was relatively reduced, which is an indication of decreased passivation capabilities. This result was in line with the reduced protection potential (Epp) of this alloy and the slight increase in corrosion rate. Furthermore, the passivation region (roughly between Epp and Epit) shifted to higher current densities, indicating a deterioration in passivation abilities [40]. Altogether, the results of cyclic potentiodynamic polarization suggests that the addition of 0.8%Mn to Zn−2%Fe alloy tendes to destabilize the passivation process and consequently may increase the sensitivity to corrosion attack [39].

The SSRT analysis was carried out considering the inherent tensile properties of the tested alloys in terms of yield point (YP), ultimate tensile strength (UTS) and elongation as examined by the authors in a previous paper [33]. This has revealed the following average measurements for Zn−2%Fe

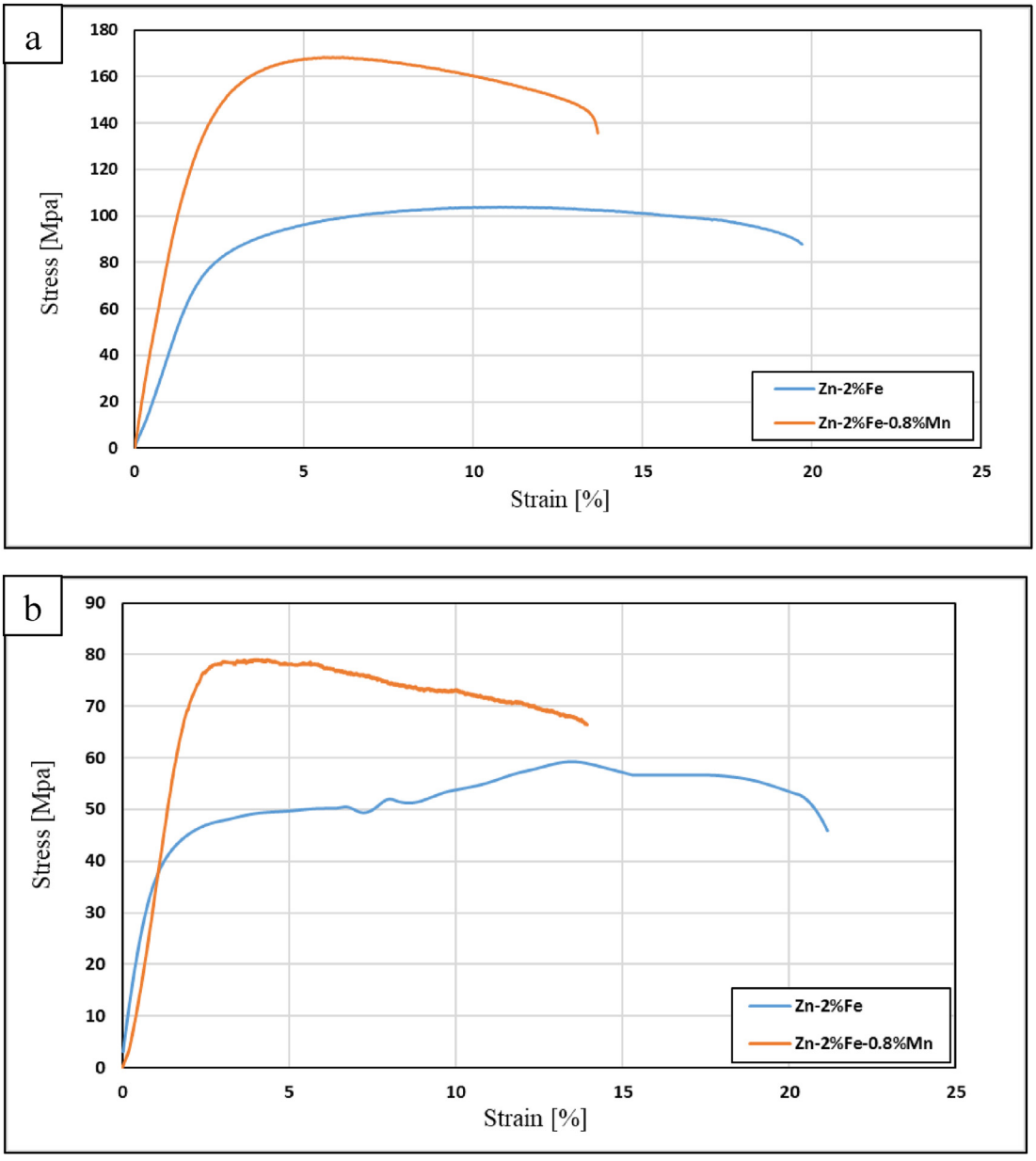

Fig. 5 − SSRT analysis in terms of stress-strain curves in PBS solution at 37 °C at strain rate of (a) 2.5 × 10^{-5} s^{-1} and (b) 2.5 × 10^{-7} s^{-1}.

and Zn–2%Fe–0.8%Mn alloys respectively; YP: 69 vs. 191 MPa, UTS: 119 vs. 224 MPa and elongation 13 vs. 8.1%. Typical stress corrosion examinations in terms of slow strain rate testing (SSRT) are shown in Fig. 5. Both alloys were tested in simulated in-vivo conditions using two different strain rates, 2.5×10^{-5} and 2.5×10^{-7} s^{-1}, which represent a very short and very long exposure time to the corrosive environment, respectively. The strengthening effect of Mn [33] was clear in both strain rates as manifested by an increased strength and reduced ductility. It was also evident that the strength of the two alloys was significantly decreased at the lower strain rate (2.5×10^{-7} s^{-1}), which is a clear indication of their sensitivity to stress corrosion conditions.

The correlation between Youngs modulus, YP, and UTS vs. strain rate is shown in Fig. 6 (a), (b) and (c) respectively. A more pronounced deterioration in the mechanical strength of Zn–2%Fe–0.8%Mn alloy compared to its reference alloy is apparent at the reduced strain rate (2.5×10^{-7} s^{-1}). The large deviation in the elongation vs. strain rate at both strain rates, as shown in Fig. 6(d), may indicate that the inherent differences in ductility between the two alloys was relatively maintained. The time to failure (TTF) vs. strain rate, as shown in Fig. 6(e), demonstrates a similar performance of the two alloys at high strain rate (2.5×10^{-5} s^{-1}) and a sharp reduction in the mean TTF of the 0.8%Mn-containing alloy at low strain rate (2.5×10^{-7} s^{-1}) (205 vs. 285 hrs). The significant difference between the two alloys in terms of TTF at reduced strain rate demonstrates that the 0.8%Mn-containing alloy was more sensitive to stress corrosion attack.

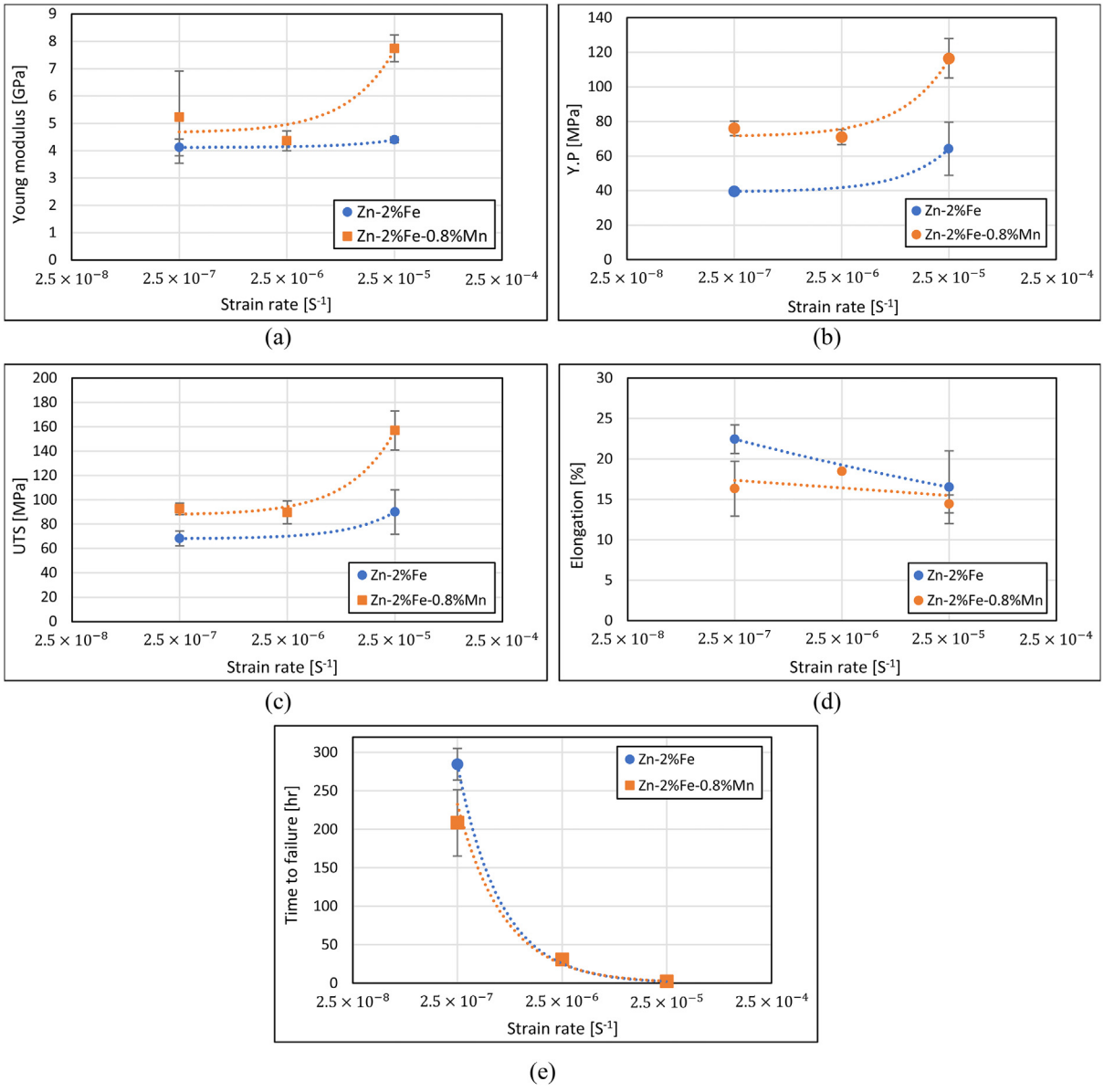

Fig. 6 – The effect of strain rate on: (a) Young modulus; (b) Y.P; (c) UTS; (d) Elongation; (e) Time to failure.

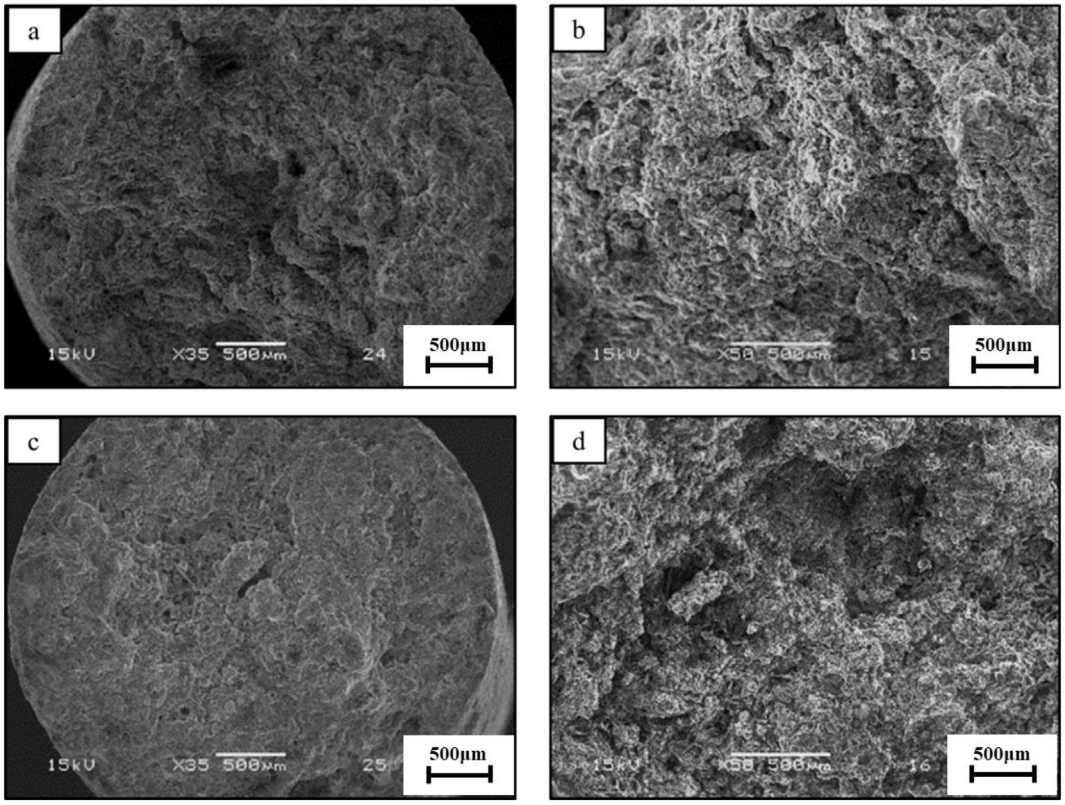

Fig. 7 – Fractography analysis post SSRT at a strain rate of $2.5*10^{-7}$ (a) and (b) Zn–2%Fe, (c) and (d) Zn–2%Fe-0.8%Mn.

The fractography analysis of the tested alloys post SSRT at a low strain rate of 2.5×10^{-7} s^{-1} is shown in Fig. 7. Although the brittle fractures of both alloys were inter-granular in nature, as expected from Zn-base alloys [20], the fracture of the alloy without Mn was relatively more ductile. This can be attributed mainly to the inherent strengthening effect of Mn that consequently increases brittleness.

The performance of Zn–2%Fe and Zn–2%Fe–0.8%Mn alloys in terms of S–N curves in air and PBS solution is shown in Fig. 8. Although both alloys showed quite similar fatigue performance in air atmosphere, a significant difference was observed in their behavior in the simulated physiological environment. This was clearly demonstrated by the substantial reduction in the fatigue endurance that was only 377,552 cycles to failure in the case of Zn–2%Fe–0.8%Mn alloy compared to 4,997,285 cycles for the Zn–2%Fe alloy under the same loading conditions. This result is in accordance with the SSRT analysis that highlighted the detrimental effect of Mn on the stress corrosion resistance of Zn–2%Fe alloy.

The fractography analysis of the tested alloys after fatigue failure in PBS solution is presented in Fig. 9. The Zn–2%Fe alloy fracture has a typical morphology of a "fisheye" failure with crack initiation sites shown at the top side and overload area at the bottom [41]. The fracture surface of Zn–2%Fe–0.8% Mn alloy was significantly more brittle with multiple crack initiating sites. This can be attributed to the increased sensitivity to localized corrosion attack generated by the Mn addition, as indicated by the potentiodynamic polarization analysis.

The direct cytotoxicity analysis of Zn–2%Fe and Zn–2% Fe–0.8%Mn was carried out using Ti–6Al–4V as a reference substance. The ability of cells to adhere to the surface of the metal while maintaining their viability is a critical requirement for the alloy to perform as a biodegradable medical implant. The adherent cells on the surfaces of the tested alloys 24 and 48 h post incubation are presented in Figs. 10–12 where green color identifies living and red color identifies dead cells. In addition, the total number of adherent cells per unit area is shown in Fig. 13. Although cells per unit field were reduced on both Zn-based alloys compared to the Ti-base alloy, the addition of 0.8%Mn to Fe–2%Zn alloy has a beneficial effect on cell growth, particularly after 48hrs of incubation. Even though fewer cells adhered to the tested alloys compared to the reference alloy, their increased numbers over time demonstrates cells were viable and able to multiply, in particular on the Zn–2%Fe–0.8%Mn alloy surface. This indicates an acceptable biocompatibility of the tested alloy with the addition of Mn.

4. Discussion

Zinc-bases arterial implants that degrade too slowly have been found to promote fibrous encapsulation [16,17], an undesirable biological response that is common to biostable

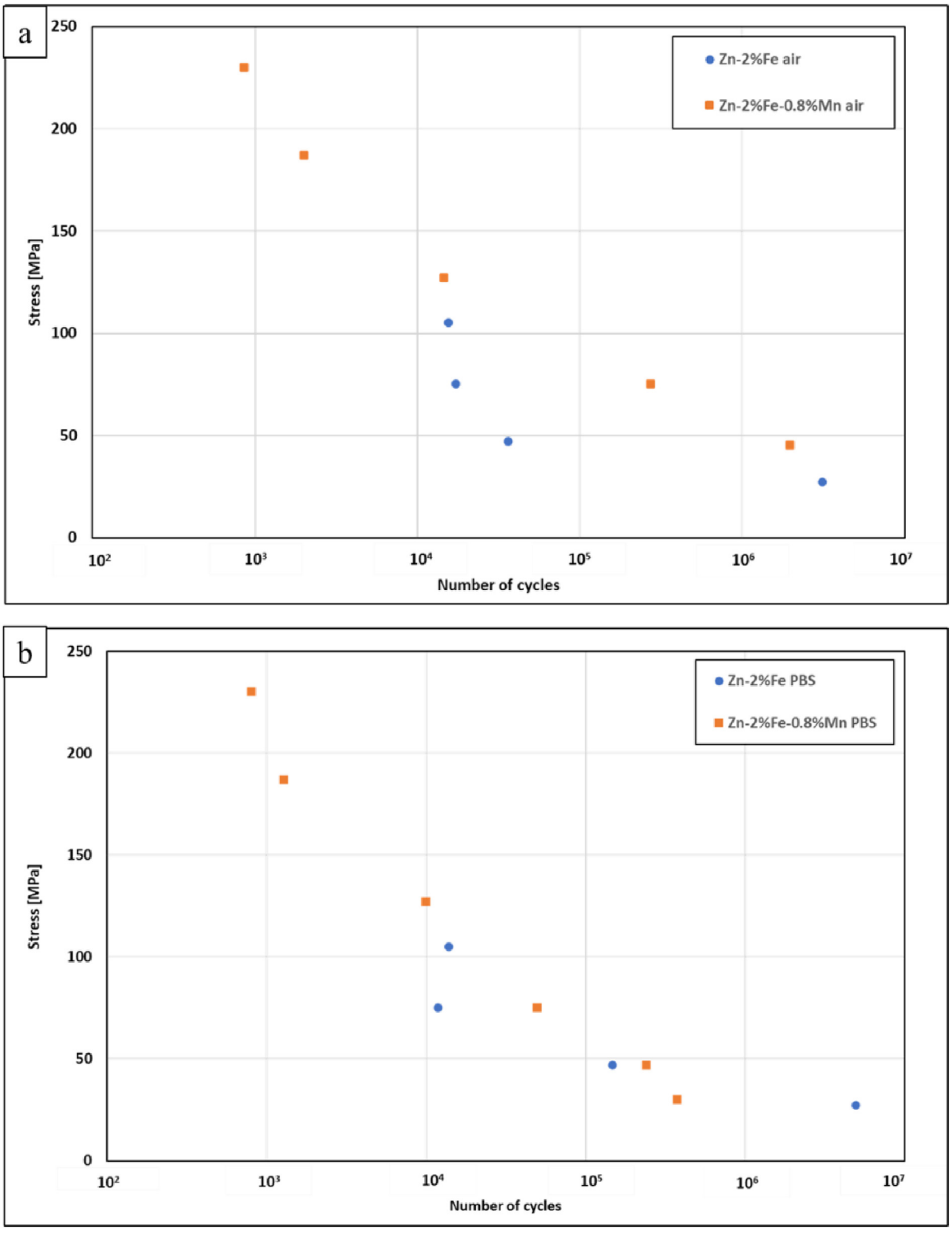

Fig. 8 – S–N curves of the tested alloys in (a) air environment and (b) PBS environment.

implants. To improve the biological integration of Zn-based implants, we recently incorporated alloying elements that can induce galvanic corrosion, such as Zn-Fe [18,19]. In the present study, we have found that the addition of 0.8%Mn to our recent Zn–2%Fe alloy has a damaging effect on the passivation capability. This can be expected to increase the corrosion rate of the alloy and potentially mitigate fibrous encapsulation responses. Relating to detrimental effect of Mn on passivation ability, and although this outcome seems to be in some disagreement with the general perception that

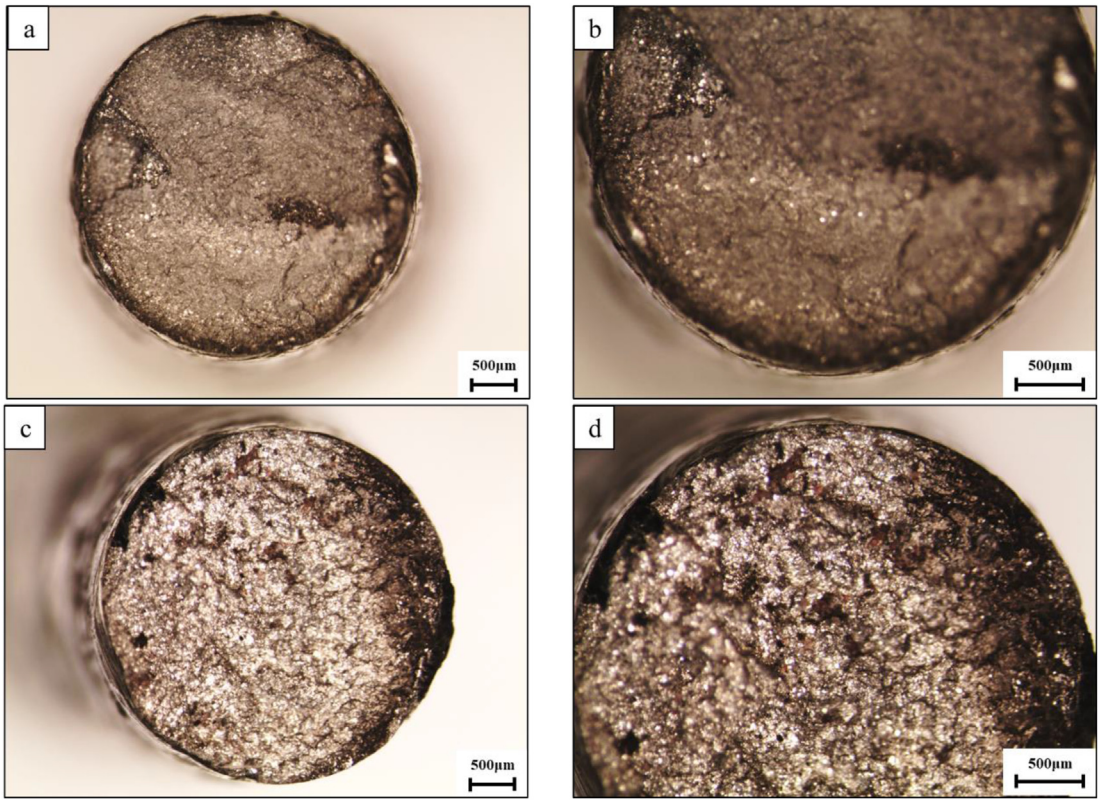

Fig. 9 – Fractography analysis after fatigue failure in PBS environment (a) and (b) Zn–2%Fe; (c) and (d) Zn–2%Fe–0.8%Mn.

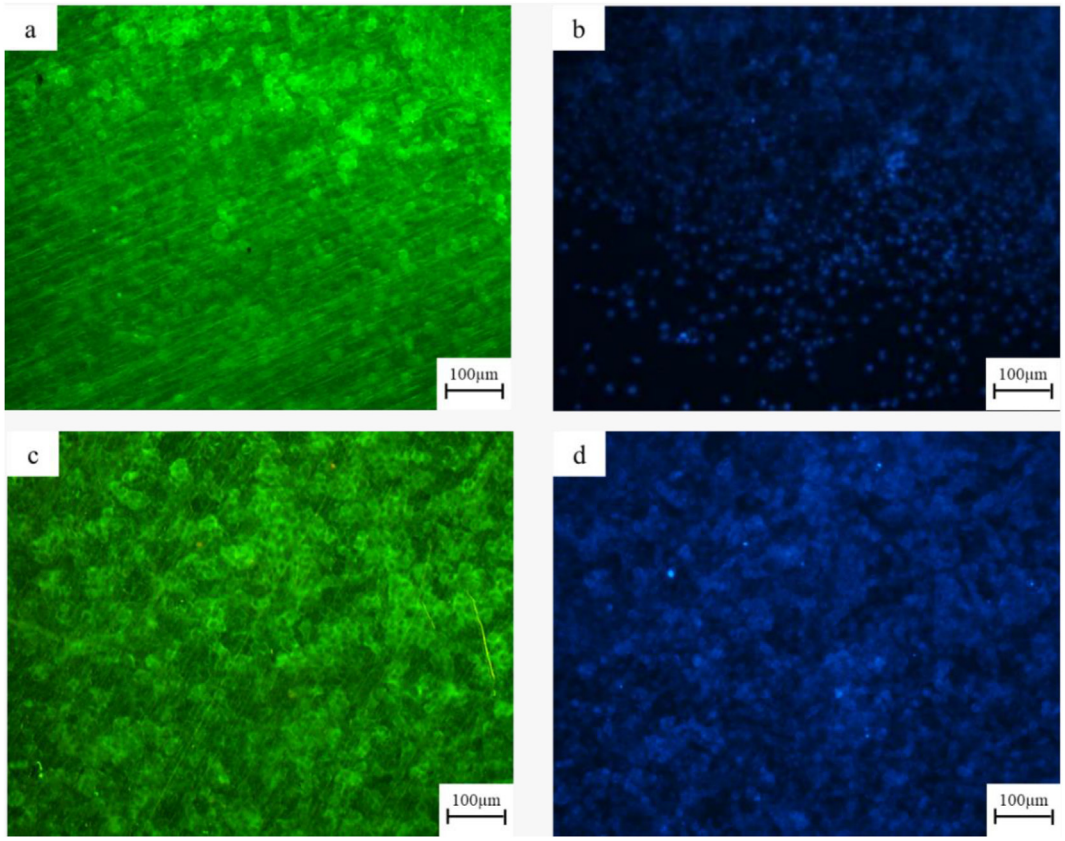

Fig. 10 – Direct cell viability on Ti–6Al–4V alloy (a, b) 24hr post incubation; (c, d) 48hr post incubation.

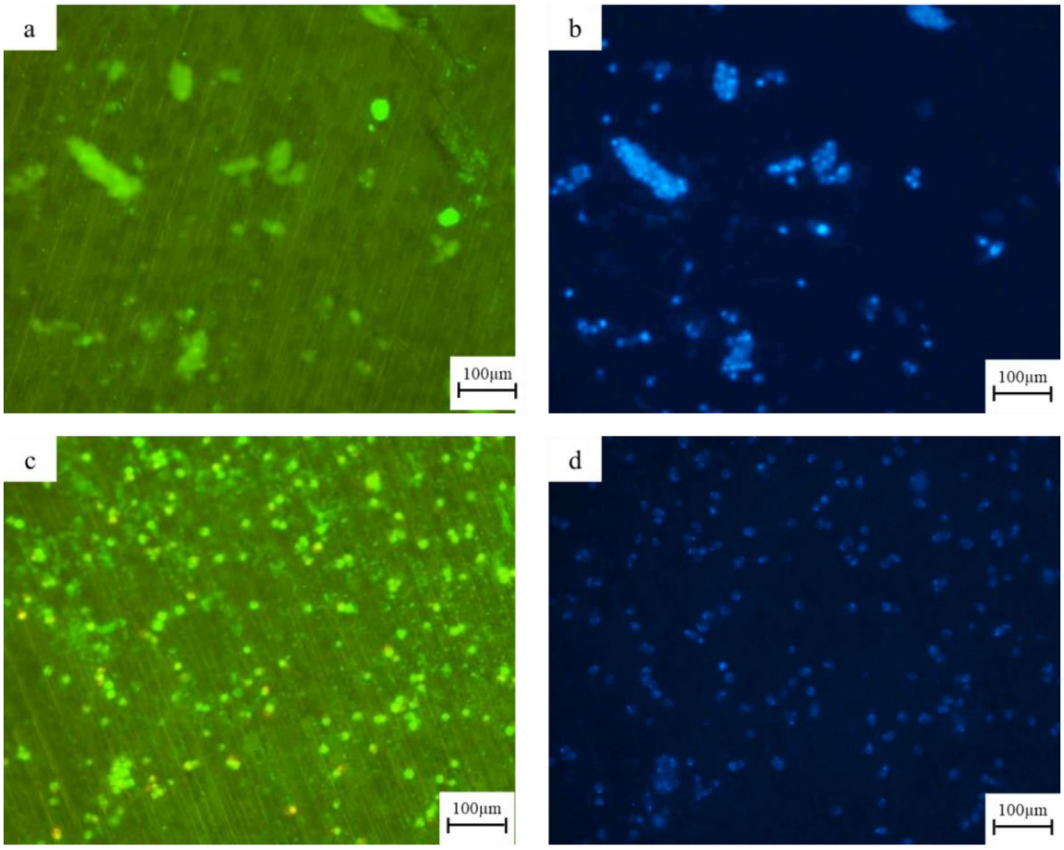

Fig. 11 – Direct cell viability on Zn–2%Fe alloy (a, b) 24hr post incubation; (c, d) 48hr post incubation.

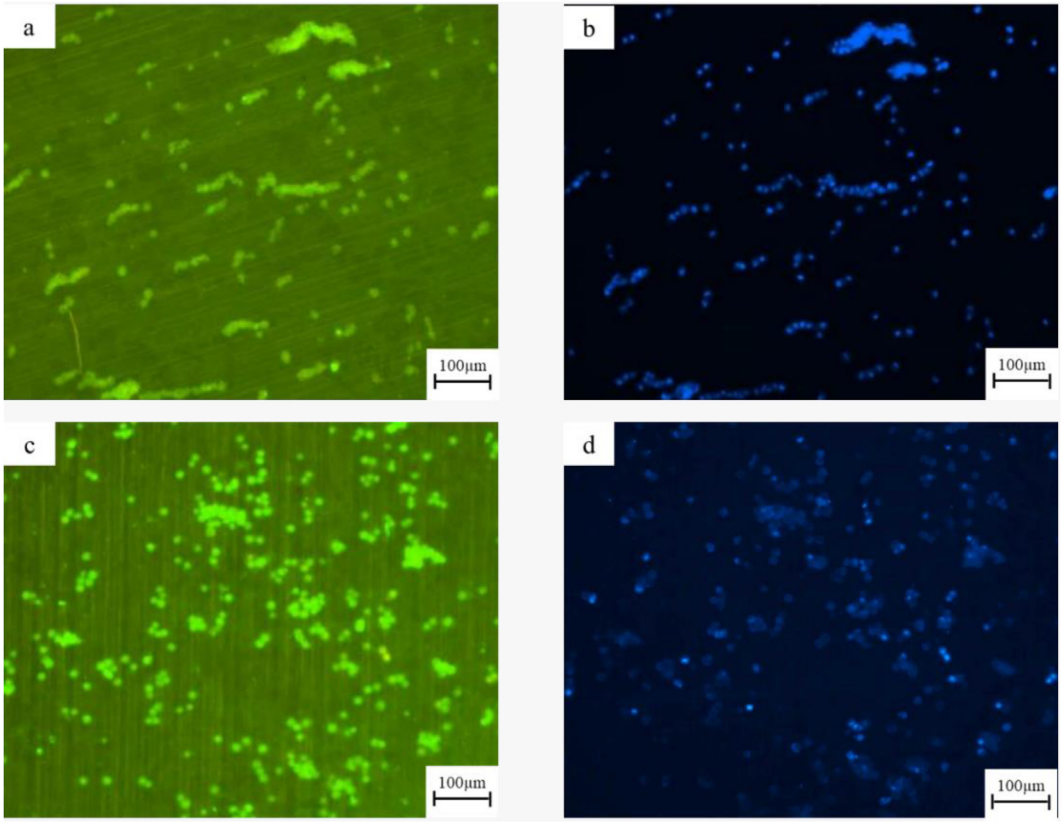

Fig. 12 – Direct cell viability on Zn–2%Fe–0.8%Mn alloy (a, b) 24hr post incubation; (c, d) 48hr post incubation.

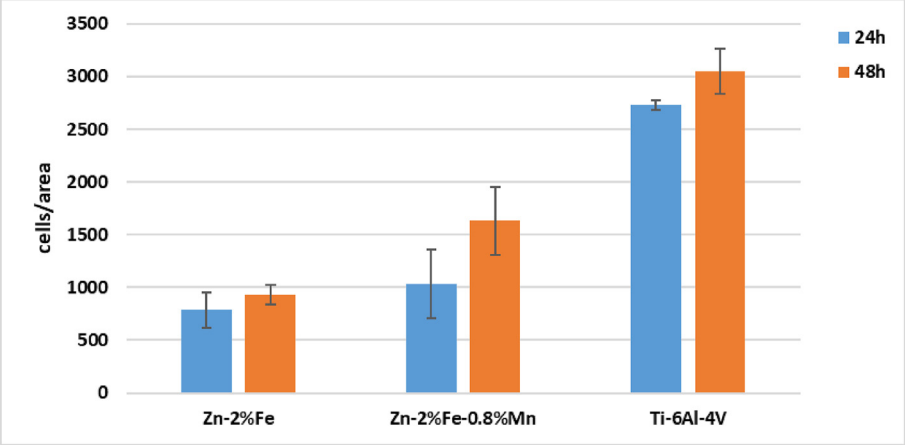

Fig. 13 – Number of cells per area post incubation after 24 and 48 h of exposure.

addition of Mn to pure Zn has a beneficial effect on corrosion resistance [46–48], the tested alloy here also includes 2%Fe which can alter this perception. For example, this was demonstrated by the TEM analysis which showed an abnormal amount of Mn (3%) that segregated to the interface between the δ phase (Fe_xZn_y) and the matrix. Owing to the significant differences in standard potential between Mn and Zn, −1.18 V and −0.763 V respectively, the preferred segregation of Mn may create an additional micro-galvanic effect that can disrupt normal passivation.

A reduction in corrosion resistance and passivation capabilities obtained by the immersion test and cyclic potentiodynamic polarization analysis can explain the reduced stress corrosion and corrosion fatigue resistance relative to the reference alloy The SSRT analysis also showed a significant reduction in time to failure (TTF) at low strain rate (205 h. vs. 285 hr.) for the alloy containing 0.8%Mn. This phenomenon was further demonstrated by the corrosion fatigue analysis in terms of S–N curves in PBS solution. We found a sharp reduction in fatigue endurance of the Zn–2%Fe alloy from nearly 5 million cycles to less than 400,000 cycles for the same alloy with 0.8% Mn. The fractography analysis for both SSRT and corrosion fatigue tests further demonstrated that the addition of 0.8%Mn to Zn–2%Fe alloy increased brittleness and consequently premature failure. Thus, modifications to the implant material with the aim to reduce fibrous encapsulation may lead to reduced corrosion stress and fatigue resistance.

The relatively reduced passivation ability and subsequently increased sensitivity to localized corrosion attack of Zn–2%Fe–0.8%Mn alloy can be mainly attributed to the presence of the secondary phases (Fe, Mn) Zn_{13} that accompany the inherent precipitate of Zn–2%Fe alloy in the form of $Zn_{11}Fe$ [19,20] and $Zn_{126}Fe_{13}$. The formation of (Fe, Mn) Zn_{13} phase mainly relates to the similarities between Fe and Mn in terms of crystal structure and atomic radius. Both elements have a BCC structure with about 3% differences in atomic radius (161 p.m. vs. 156 p.m.), which enables Mn to replace some of the Fe atoms in this phase.

The direct cell viability assessment of this study is in accordance with the indirect cell viability analysis from a previous study by the authors [33]. In both cases the addition of 0.8%Mn to the base Zn–2%Fe alloy had a favorable effect on cell viability. This was demonstrated by the relatively increased number of adherent cells per unit area in Zn–2%Fe-0.8%Mn alloy (Fig. 13) and by cell viability of 95–120% after 24 and 48 post incubation. In both studies the favorable effect of Mn on cell viability was more dominant after 48 h post incubation, which emphasizes the positive effect of Mn. In general, our results are in accordance with the findings of Prasadh et al. [42] and Wang et al. [43] who found a favorable effect of Mn on cell viability in Mg–2%Zn–1%Mn and Mg–Zn–Ca alloys, respectively. The cell viability results in tandem with the reduced passivation effectiveness, suggest that the biocompatibility of a Zn–2%Fe–0.8%Mn arterial implant may be superior to that of the Zn–2%Fe reference alloy, even though considerable mechanical performance has been sacrificed. Future work could focus on uniformly distributing nano-sized secondary phases to improve corrosion uniformity.

Overall, the results of this study demonstrate the potential of Zn–2%Fe–0.8%Mn alloy to serve as a biodegradable structural implant material. The addition of 0.8%Mn improves the specific strength and the direct cell viability of the Zn–2%Fe alloy. However, it also reduces the passivation capability and consequently the stress corrosion and corrosion fatigue resistance. This practically means that the potential application of biodegradable Zn–2%Fe-0.8%Mn alloy in implants that are exposed to stress corrosion and corrosion fatigue conditions should be done in caution to avoid premature failure. Hence additional in-vivo examinations are essential to confirm the potential of using this alloy in medical applications.

5. Conclusions

Although the addition of 0.8%Mn to Zn–2%Fe alloy has a favorable effect on strength and direct cell viability under in-

vitro conditions, it is accompanied by increased sensitivity to localized corrosion attack and reduced passivation capabilities. Consequently, the stress corrosion resistance at slow strain rate tension and under cyclic loading is decreased particularly in terms of time to failure (TTF) and fatigue endurance, respectively.

Declaration of competing interest

The authors declare that they have no known competing financial interests or personal relationships that could have appeared to influence the work reported in this paper.

REFERENCES

[1] Zhuo X, Wu Y, Ju J, Liu H, Jiang J, Hu Z, et al. Recent progress of novel biodegradable zinc alloys: from the perspective of strengthening and toughening. J Mater Res Technol 2022;17:244–69. https://doi.org/10.1016/j.jmrt.2022.01.004.

[2] Staiger M, Pietak A, Huadmai J, Biomaterials GD, undefined. Magnesium and its alloys as orthopedic biomaterials: a review. Elsevier. (n.d.). 2006. [Accessed 23 June 2022], https://www.sciencedirect.com/science/article/pii/S0142961205009014.

[3] Aghion E, Bronfin B, Eliezer D, Von Buch F, Schumann S, Friedrich HE. The art of developing new magnesium alloys for high temperature applications, Trans Tech Publ (n.d.). 2003. [Accessed 5 July 2022], https://www.scientific.net/MSF.419-422.407.pdf.

[4] Ghali E, Dietzel W, Kainer KU. General and localized corrosion of magnesium alloys: a critical review. J Mater Eng Perform 2004;13:7–23. https://doi.org/10.1361/10599490417533.

[5] Zberg B, Uggowitzer PJ, Löffler JF. MgZnCa glasses without clinically observable hydrogen evolution for biodegradable implants. Nat Mater 2009;8. https://doi.org/10.1038/nmat2542.

[6] Tong X, Zhu L, Wu Y, Song Y, Wang K, Huang S, et al. A biodegradable Fe/Zn–3Cu composite with requisite properties for orthopedic applications. Acta Biomater 2022;146:506–21. https://doi.org/10.1016/j.actbio.2022.04.048.

[7] Wątroba M, Bednarczyk W, Szewczyk PK, Kawałko J, Mech K, Grünewald A, et al. In vitro cytocompatibility and antibacterial studies on biodegradable Zn alloys supplemented by a critical assessment of direct contact cytotoxicity assay. J Biomed Mater Res B Appl Biomater 2023;111:241–60. https://doi.org/10.1002/jbm.b.35147.

[8] Di T, Xu Y, Liu D, Sun X. Microstructure, mechanical performance and anti-bacterial activity of degradable Zn-Cu-Ag alloy. Metals 2022;12. https://doi.org/10.3390/met12091444.

[9] Levy GK, Goldman J, Aghion E. The prospects of zinc as a structural material for biodegradable implants—a review paper. Metals 2017;7. https://doi.org/10.3390/met7100402.

[10] Plum LM, Rink L, Hajo H. The essential toxin: impact of zinc on human health. Int J Environ Res Publ Health 2010;7:1342–65. https://doi.org/10.3390/ijerph7041342.

[11] Li H, Yang H, Zheng Y, Zhou F, Qiu K, Wang X. Design and characterizations of novel biodegradable ternary Zn-based alloys with IIA nutrient alloying elements Mg, Ca and Sr. Mater Des 2015;83. https://doi.org/10.1016/j.matdes.2015.05.089.

[12] Wang K, Tong X, Lin J, Wei A, Li Y, Dargusch M, et al. Binary Zn–Ti alloys for orthopedic applications: corrosion and degradation behaviors, friction and wear performance, and cytotoxicity. J Mater Sci Technol 2021;74. https://doi.org/10.1016/j.jmst.2020.10.031.

[13] Prakash C, Singh S, Verma K, Sidhu SS, Singh S. Synthesis and characterization of Mg-Zn-Mn-HA composite by spark plasma sintering process for orthopedic applications. Vacuum 2018;155. https://doi.org/10.1016/j.vacuum.2018.06.063.

[14] Liu X, Sun J, Zhou F, Yang Y, Chang R, Qiu K, et al. Micro-alloying with Mn in Zn-Mg alloy for future biodegradable metals application. Mater Des 2016;94. https://doi.org/10.1016/j.matdes.2015.12.128.

[15] Lin J, Tong X, Wang K, Shi Z, Li Y, Dargusch M, et al. Biodegradable Zn–3Cu and Zn–3Cu–0.2Ti alloys with ultrahigh ductility and antibacterial ability for orthopedic applications. J Mater Sci Technol 2021;68. https://doi.org/10.1016/j.jmst.2020.06.052.

[16] Yue R, Huang H, Ke G, Zhang H, Pei J, Xue G, et al. Microstructure, mechanical properties and in vitro degradation behavior of novel Zn-Cu-Fe alloys. Mater Char 2017;134:114–22. https://doi.org/10.1016/j.matchar.2017.10.015.

[17] Guillory RJ, Bowen PK, Hopkins SP, Shearier ER, Earley EJ, Gillette AA, et al. Corrosion characteristics dictate the long-term inflammatory profile of degradable zinc arterial implants. ACS Biomater Sci Eng 2016;2:2355–64. https://doi.org/10.1021/acsbiomaterials.6b00591.

[18] Kafri A, Ovadia S, Yosafovich-Doitch G, Aghion E. In vivo performances of pure Zn and Zn–Fe alloy as biodegradable implants. J Mater Sci Mater Med 2018;29. https://doi.org/10.1007/S10856-018-6096-7.

[19] Kafri A, Ovadia S, Yosafovich-Doitch G, Aghion E. The effects of 4%Fe on the performance of pure zinc as biodegradable implant. Material, Ann Biomed Eng. 2019. https://doi.org/10.1007/s10439-019-02245-w.

[20] Avior O, Ben Ghedalia-Peled N, Ron T, Goldman J, Vago R, Aghion E. Stress corrosion analysis and direct cell viability of biodegradable Zn-Fe-Ca alloy in in-vitro conditions. Metals 2022;12. https://doi.org/10.3390/met12010076.

[21] Li HF, Shi ZZ, Wang LN. Opportunities and challenges of biodegradable Zn-based alloys. J Mater Sci Technol 2020;46:136–8. https://doi.org/10.1016/j.jmst.2019.12.014.

[22] Törne K, Örnberg A, Weissenrieder J. Influence of strain on the corrosion of magnesium alloys and zinc in physiological environments. Acta Biomater 2017;48:541–50. https://doi.org/10.1016/j.actbio.2016.10.030.

[23] Ferrigno B, Bordett R, Duraisamy N, Moskow J, Arul MR, Rudraiah S, et al. Bioactive polymeric materials and electrical stimulation strategies for musculoskeletal tissue repair and regeneration. Bioact Mater 2020;5:468–85. https://doi.org/10.1016/j.bioactmat.2020.03.010.

[24] Li G, Yang H, Zheng Y, Chen XH, Yang JA, Zhu D, et al. Challenges in the use of zinc and its alloys as biodegradable metals: perspective from biomechanical compatibility. Acta Biomater 2019;97. https://doi.org/10.1016/j.actbio.2019.07.038.

[25] Dietary reference intakes for vitamin A, vitamin K, arsenic, boron, chromium, copper, iodine, iron, manganese, molybdenum, nickel, silicon, vanadium, and zinc. 2001. https://doi.org/10.17226/10026.

[26] Solomons NW, Ruz M. Trace element requirements in humans: an update. J Trace Elem Exp Med 1998;11. 1998)11:2/3<177::AID-JTRA9>3.0.CO;2-5, https://doi.org/10.1002/(SICI)1520-670X.

[27] Huang T, Cheng J, Zheng YF. In vitro degradation and biocompatibility of Fe-Pd and Fe-Pt composites fabricated by spark plasma sintering. Mater Sci Eng C 2014;35. https://doi.org/10.1016/j.msec.2013.10.023.
[28] Encyclopedia of dietary supplements. 2010. https://doi.org/10.1201/b14669.
[29] Present knowledge in nutrition. 2012. https://doi.org/10.1002/9781119946045.
[30] Soetan KO, Olaiya CO, Oyewole OE. The importance of mineral elements for humans , domestic animals and plants : a review. Afr J Food Sci 2010;4.
[31] Shi ZZ, Li ZL, Bai WS, Tuoliken A, Yu J, Liu XF, Fe Mn. Zn13 phase and its core-shell structure in novel biodegradable Zn-Mn-Fe alloys. Mater Des 2019;162. https://doi.org/10.1016/j.matdes.2018.11.057.
[32] Shi Z, Yu J, X.L M, Design, undefined. Microalloyed Zn-Mn alloys: from extremely brittle to extraordinarily ductile at room temperature. Elsevier. (n.d.) [Accessed 21 June 2022]. https://www.sciencedirect.com/science/article/pii/S0264127518301394.
[33] Ben Tzion-Mottye L, Ron T, Eliezer D, Aghion E. The effect of Mn on the mechanical properties and in vitro behavior of biodegradable Zn-2%Fe alloy. Metals 2022;12. https://doi.org/10.3390/met12081291.
[34] Biological evaluation of medical devices —Part 5: tests for in vitro cytotoxicity. In: ANSI/AAMI/ISO 10993-5:2009/(R) 2014; biological evaluation of medical devices —Part 5: tests for in vitro cytotoxicity; 2009. https://doi.org/10.2345/9781570203558.ch1.
[35] Biological evaluation of medical devices — Part 12: sample preparation and reference materials. In: ANSI/AAMI/ISO 10993-12:2012; biological evaluation of medical devices — Part 12: sample preparation and reference materials; 2012. https://doi.org/10.2345/9781570204500.ch1.
[36] S. Bhan, A. La, S. Sbagh, Phase diagram evaluations: section II the Fe-Mn-Zn system (Iron-Manganese-Zinc), n.d.
[37] Okamoto NL, Tanaka K, Yasuhara A, Inui H. Structure refinement of the δ1p phase in the Fe-Zn system by single-crystal X-ray diffraction combined with scanning transmission electron microscopy. Acta Crystallogr B Struct Sci Cryst Eng Mater 2014;70:275–82. https://doi.org/10.1107/S2052520613034410.
[38] Belin CHE, Belin RCH. Synthesis and crystal structure determinations in the Γ and δ phase domains of the iron-zinc system: electronic and bonding analysis of Fe13Zn39 and FeZn10, a subtle deviation from the Hume-Rothery standard? J Solid State Chem 2000;151. https://doi.org/10.1006/jssc.2000.8626.
[39] W.H. Peter, R.A. Buchanan, C.T. Liu, P.K. Liaw, M.L. Morrison, J.A. Horton, C.A. Carmichael, J.L. Wright, Localized corrosion behavior of a zirconium-based bulk metallic glass relative to its crystalline state, n.d.
[40] Dai N, Zhang LC, Zhang J, Chen Q, Wu M. Corrosion behavior of selective laser melted Ti-6Al-4 V alloy in NaCl solution. Corrosion Sci 2016;102:484–9. https://doi.org/10.1016/j.corsci.2015.10.041.
[41] Li H, Huang Y, Ji X, Wen C, Wang LN. Fatigue and corrosion fatigue behaviors of biodegradable Zn-Li and Zn-Cu-Li under physiological conditions. J Mater Sci Technol 2022;131. https://doi.org/10.1016/j.jmst.2022.04.051.
[42] Prasadh S, Gupta M, Wong R. In vitro cytotoxicity and osteogenic potential of quaternary Mg-2Zn-1Ca/X-Mn alloys for craniofacial reconstruction. Sci Rep 2022;12. https://doi.org/10.1038/s41598-022-12490-0.
[43] Wang J, Huang S, Li Y, Wei Y, Xi X, K.C.-M.S. and, undefined. Microstructure, mechanical and bio-corrosion properties of Mn-doped Mg–Zn–Ca bulk metallic glass composites. Elsevier2013 ; (n.d.) [Accessed 23 June 2022], https://www.sciencedirect.com/science/article/pii/S0928493113003081.
[44] Raghavan V. Phase diagram Fe-Mn-Zn. J Phase Equil 2003;24(6):556–7.
[45] Lee HH, Hiam D. Corrosion resistance of galvannealed steel. Corrosion 1989;45.10:852–6.
[46] Jia B, Yang H, Han Y, Zhang Z, Qu X, Zhuang t, et al. In Vitro and in vivo studies of Zn-Mn biodegradable metals designed for orthopedic applications. Acta Biomater 2020;108:358–72.
[47] Bagha PS, Khaleghpanah S, Sheibani S, Khakbiz M, Zakeri A. Characterization of nanostructured biodegradable Zn-Mn alloy synthesized by mechanical alloying. J Alloys Compd 2018;735:1319–27.
[48] Sun J, Zhanga X, Shib ZZ, X Gaob X, Liub XF, Wanga JQ, et al. Adjusting comprehensive properties of biodegradable Zn-Mn alloy through. Mater Today Commun 2020;23:101150.